

Article

Multi-Scale Interaction between a Squall Line and a Supercell and Its Impact on the Genesis of the “0612” Gaoyou Tornado

Jiajia Tang ^{1,2} , Xiaowen Tang ^{1,2,*}, Fen Xu ³ and Fugui Zhang ^{1,2}

¹ School of Meteorological Observation, Chengdu University of Information Technology, Chengdu 610225, China; 3190302034@stu.cuit.edu.cn (J.T.); zfg@cuit.edu.cn (F.Z.)

² CMA Key Laboratory of Atmospheric Sounding, Chengdu 610225, China

³ Nanjing Joint Institute for Atmospheric Sciences, Nanjing 210009, China; xufen1130@tom.com

* Correspondence: xtang@cuit.edu.cn

Abstract: The interaction between a squall line and a supercell and its impact on the genesis of a tornado that occurred in Gaoyou, Jiangsu Province, China on 12 June 2020 were analyzed using multi-source observations. The tornado formed as the result of an intensified meso- γ supercell in a favorable large-scale environment. The supercell developed in front of a squall line and slowly intensified after its formation. Due to its small size and weak intensity, the supercell did not produce any severe weather before the approaching of the squall line. As the squall line entered its mature stage with the formation of a well-organized bow echo, the supercell in front of the bow echo began to rapidly intensify and finally led to the tornado touchdown. The analysis of mesoscale and storm-scale wind fields indicated that the bow echo of the approaching squall line modified the kinematic fields near the supercell in such a way that was favorable for the intensification of the supercell. The interaction between the squall line and the supercell may have played a critical role in the occurrence of this tornado.



Citation: Tang, J.; Tang, X.; Xu, F.; Zhang, F. Multi-Scale Interaction between a Squall Line and a Supercell and Its Impact on the Genesis of the “0612” Gaoyou Tornado. *Atmosphere* **2022**, *13*, 272. <https://doi.org/10.3390/atmos13020272>

Academic Editors: Tinghai Ou, Xuejia Wang and Hengde Zhang

Received: 30 December 2021

Accepted: 3 February 2022

Published: 5 February 2022

Publisher’s Note: MDPI stays neutral with regard to jurisdictional claims in published maps and institutional affiliations.



Copyright: © 2022 by the authors. Licensee MDPI, Basel, Switzerland. This article is an open access article distributed under the terms and conditions of the Creative Commons Attribution (CC BY) license (<https://creativecommons.org/licenses/by/4.0/>).

Keywords: tornado; squall line; bow echo; supercell; storm interaction

1. Introduction

Tornadoes are the most violent atmosphere storms which have been recorded on all continents except Antarctica. The United States of America has the highest frequency of tornado occurrence with about 1200 tornadoes each year [1]. Despite much lower annual occurrence of tornadoes in China [2], they often cause serious fatalities and economic losses due to China’s large population. With the advance of observation infrastructure and the social media based on smartphones, more high-impact tornadoes in China have been reported in recent years. An enhanced Fujita scale 3 (EF3) tornado spawned by the outer rainband of Typhoon Mujigae hit Foshan, Guangdong Province on 4 October 2015, leaving a 31 km long damage swath [3]. An EF4 tornado occurred in Funing County, Jiangsu Province on 23 June 2016, causing 98 fatalities and 846 injuries [4]. The growing public concern has driven a rapid increase in research and operational forecasting regarding tornadoes in China.

Due to their small spatial scales, it is difficult to directly identify tornadoes using in situ observations [5–7]. Weather radars are the most important tool in monitoring and understanding tornadoes. Early conventional radars related the occurrence of tornado to supercell storms, or more specifically the hook echo of supercells [8,9]. With the advent of Doppler radar capable of velocity measurement, mesocyclone [10] and tornadic vortex signature (TVS) [11] associated with supercells were identified and studied. Corresponding algorithms were developed and applied in operational tornado warning [12,13]. Supercells are the most studied parent storm [14] of tornadoes partly due to the fact that they produce the majority of tornadoes [15]. Despite the wide recognition in research and operation, neither the hook echo [16] nor the mesocyclone [17] was shown to be a reliable indicator for

the occurrence of tornadoes. Due to the “horizon” and “aspect ratio” problems of weather radars [18], the maximum detection range of TVSs is limited to 100 km even for large tornadoes (1–2 km).

Tornadoes developed from non-supercell storms were usually small, weak, and short-lived [19,20], which makes it even more difficult to detect. According to tornado statistics [14], the majority of non-supercell tornadoes occurred in quasi-linear convective systems (QLCSs), e.g., squall lines and bow echoes. These tornadoes were generally associated with complex interactions between convective systems of different scales. Funk et al. [21] showed that tornadoes were produced on the apex of the most intense bow echo in a long-lived squall line. Dewald and Funk [22] documented a similar case to that of Funk et al. [21], but further noting that the occurrences of tornadoes was related to the sudden evolution of a linear convective segment to a bow echo. Trapp and Weisman [23] and Atkins and Laurent [24] showed that the meso-vortices associated with bow echoes and squall lines were closely related to the straight-line wind and tornado damages on the ground. Penn et al. [25] found that two Massachusetts supercell tornadoes each occurred in a squall line. Goodman and Knupp [26] showed that the merger of a squall line with a strong supercell led to the subsequent rapid intensification of an existing tornado. Wolf [27] documented an “unexpected evolution” of a supercell after being intercepted by a bow echo, which produced damaging winds and tornadoes afterwards. French and Parker [28] documented 21 tornadoes produced by the mergers between supercells and squall lines. The number of tornadoes that occurred relative to the time of the merger was shown to be related to the strength of synoptic forcing.

Despite the difficulty of detecting weak tornadoes, the development and interactions of their parent storms may show important precursors for their occurrences [19], therefore providing valuable guidance for operational tornado warning. Considering the fact that most tornadoes in China were weak and developed in various synoptic and geographical environments [4], it is of great importance to understand the interaction of storms associated with tornadoes in China. In this study, the environmental condition, structure, and evolution of a squall line and a supercell associated with an EF2 tornado occurred in Gaoyou, Jiangsu Province, China on 12 June 2020 were analyzed. It was shown that the interaction between the bow echo of the squall line and the supercell may be crucial for the occurrence of this tornado. The remainder of this paper is organized as follows. Section 2 introduces the data and the analysis methodologies used in this paper. Section 3 presents the analysis of the environment, structure, and evolution of the squall line and the supercell. Section 4 shows the multi-scale interaction between the squall line and the supercell and its possible impact on the tornadogenesis. Conclusions and discussions are given in Section 5.

2. Data and Methodology

2.1. Event Overview

A tornado touched down around 1355 LTC (UTC + 08) on 12 June 2020 near the Gaoyou city in East China (Figure 1a, the red cross). This area has the most frequent occurrence of tornadoes in China due to its flat terrain and the contrasting thermodynamic properties between land and sea [29]. Based on the damage survey conducted by Jiangsu Meteorological Bureau, this tornado lasted about 10 min from 1354 to 1406 LTC (Figure 1b–d) with a damage path of 1 km long and a peak width of 80 m (Figure 1e). The intensity of this tornado was estimated to be EF2.

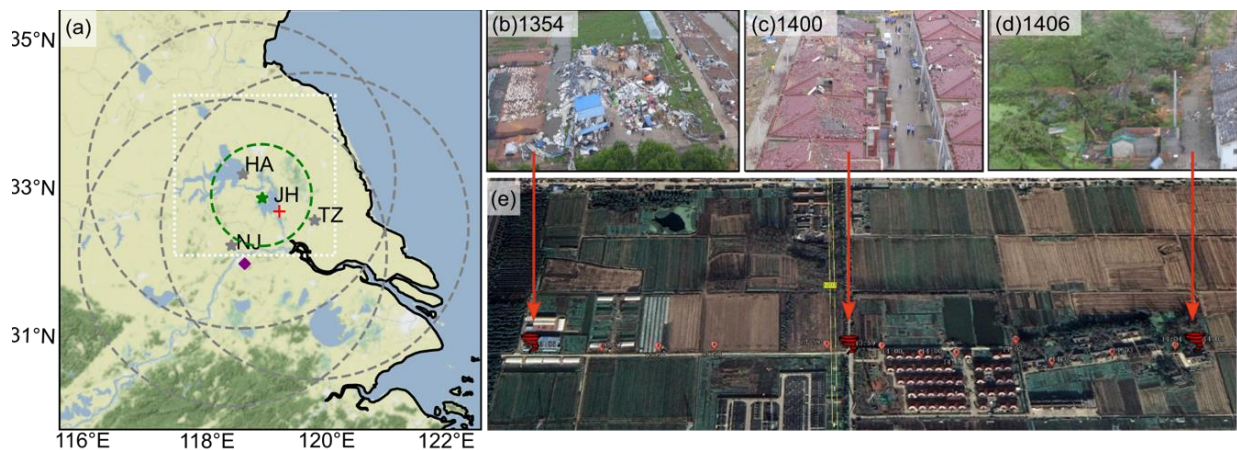


Figure 1. (a) The locations of the tornado and different observations used in this study. The gray (green) stars and the gray (green) dotted circles represent the location and the 230 km (75 km) observation radius of the S-band (X-band) radars. The red cross represents the tornado location. The purple diamond represents the NJ sounding station. The white dotted square represents the three-dimensional wind retrieval region. (b–e) The images of ground damage survey.

This tornado was observed by the Huai’an (HA), Nanjing (NJ), Taizhou (TZ) S-band doppler radars and the Jinhua (JH) X-band polarimetric radar, as shown in Figure 1a. The S-band (X-band) radars employ a 9-tilt (11-tilt) volume scan from 0.5° to 19.5° (1.5° to 11.4°) at a 6 min update. The beam width of the S-band and X-band radars are 1.0° and 0.93°, respectively. More information about these radars is listed in Table 1. Due to the complex local environment and the limitation of the radar hardware, the radar observations were subjected to non-meteorological contamination and radial velocity aliasing. To improve the reliability of the results, quality control (QC) procedures were applied to the radar volumetric observations before retrieval and analysis. An automatic QC script utilizing algorithms presented in various previous studies [30–32] was applied to remove ground clutters, freckles, velocity aliasing, and interferences. The remaining quality problems were manually inspected and removed using the National Center for Atmospheric Research (NCAR) Soloi software. The radar observations after QC were interpolated into a three-dimensional Cartesian grid with 1 km resolution in both horizontal and vertical directions for wind retrieval. The analysis domain covers an area of 240 × 240 km as shown in Figure 1a (the white dotted square) and extends to 15 km altitude. Unfortunately, the beams of the JH radar toward the south were severely blocked by buildings. The JH radar was only used to retrieve the mean wind fields. The hourly ERA5 reanalysis data (<https://cds.climate.copernicus.eu> (accessed on 1 December 2021)) and the NJ sounding data (the purple diamond in Figure 1a) were used to analyze the environmental conditions of this event.

Table 1. Information of the weather radars.

Radar	Longitude	Latitude	Band	Resolution (m)		Detection Range (km)	
				Reflectivity	Velocity	Reflectivity	Velocity
NJ	118.69	32.191	S	1000	250	460	230
TZ	119.99	32.557	S	1000	250	460	230
HA	119.02	33.62	S	1000	250	460	230
JH	119.11	32.979	X	60	60	75	75

2.2. Wind Retrieval

To analyze the environmental winds of this tornado, the DVAD (distance velocity azimuth display) [33] method was applied to the single radar volumetric observations.

DVAD uses the quantity rV_d , instead of V_d , to retrieve averaged environmental wind fields. The quantity rV_d at a point $P(x, y, z)$ observed by a Doppler radar is expressed in terms of the three-dimensional Cartesian coordinates x, y, z and the velocity components u, v, w as follows:

$$rV_d = ux + vy + (w + v_t)z \tag{1}$$

Both w and v_t in (1) are neglected because their mean values are one order of magnitude smaller than those of u and v on the spatial scale covered by a Doppler radar [34]. Representing the horizontal components u and v by finite terms of their Taylor series, the rV_d can be rewritten in a concise form using the summation notation

$$rV_d = \sum_{i=1}^n \sum_{j=0}^i c_{ij} x^{i-j} y^j \tag{2}$$

where c_{ij} is the coefficient and n is the highest degree of the two-dimensional polynomial function. The coefficients of the polynomial series are related to the mean horizontal winds by $c_{10} = u_0$ and $c_{11} = v_0$. As shown by Tang et al. [34], DVAD is able to provide robust mean wind retrievals when data contain noise and voids.

The DVAD method can only obtain averaged wind fields within a circle centered at the radar, which is insufficient to investigate the distribution and variation of convective-scale wind fields associated with the tornado. A three-dimensional variational-based method [35] utilizing multiple radar observations was used to retrieve the convective-scale wind fields. The variational retrieval aims to minimize the following cost function J

$$J = \gamma_1 J_1 + \gamma_2 J_2 + \gamma_3 J_3 + \gamma_4 J_4 + \gamma_5 J_5 \tag{3}$$

where γ_i is the weight of each sub-item of the cost function J .

The first term on the right-hand side (RHS) of Equation (3) represents the difference between the analyzed and the observed radial velocity

$$J_1 = \int \sum_i^m \left(\frac{ux_i + vy_i + (w + W_t)z_i}{r_i} - V_{ri} \right)^2 \tag{4}$$

where m is the number of radars, r_i stands for the distance from the analysis grid to the i th radar, u, v , and w are the retrieved east–west, north–south, and vertical wind components in the Cartesian coordinates x, y , and z , respectively. $W_t = 2.6Z^{0.107} \left(\frac{\rho_0}{\rho} \right)^{0.45}$ represents the terminal fall speed of precipitation particles, Z is the reflectivity, ρ is the air density, and ρ_0 is the air density at the surface.

The second term on the RHS of Equation (3) contains the anelastic continuity equation with the following form:

$$J_2 = \iiint \left(\frac{\partial u}{\partial x} + \frac{\partial v}{\partial y} + \frac{\partial w}{\partial z} \right)^2 \tag{5}$$

The third and fourth terms on the RHS of Equation (3) constrain the vertical velocity at the top and bottom layer as follows:

$$J_3 = \iint w_{top}^2 \tag{6}$$

$$J_4 = \iint w_{bottom}^2 \tag{7}$$

where w_{top} and w_{bottom} are the vertical velocity at the top and bottom boundaries, respectively.

The fifth term is a Laplacian smoothing filter, defined as follows:

$$J_5 = \iiint \left(\nabla^2 u \right)^2 + \left(\nabla^2 v \right)^2 + \left(\nabla^2 w \right)^2 \tag{8}$$

3. Observation Analysis

3.1. Synoptic Background

The weather map at 0800 LTC on 12 June 2020 showed a weak short-wave trough on 500 hPa (the brown line in Figure 2a) over East China. The southwest jets on 850 hPa (Figure 2b, the yellow contours) provided warm and moist air to the location of the tornado. Under the southwest jets, there was a low-pressure system on the surface (Figure 2c). The tornado was spawned on the north side of the southwest jets and the east boundary of the surface depression. The skew T -log P diagram and the 0–6 km hodograph (Figure 2d) from the NJ sounding deployed at 0800 LTC on 12 June 2020 showed a veering vertical wind shear (VWS). The environmental factors related to the development of supercells and tornadoes are listed in Table 2. The storm motion required for the calculation of the storm-relative helicity (SRH) was estimated based on the reflectivity field in Figure 3b. Figure 2 and Table 2 indicate that the synoptic environment was generally favorable for the development of convection, but only marginal for supercells and tornadoes [36–38].

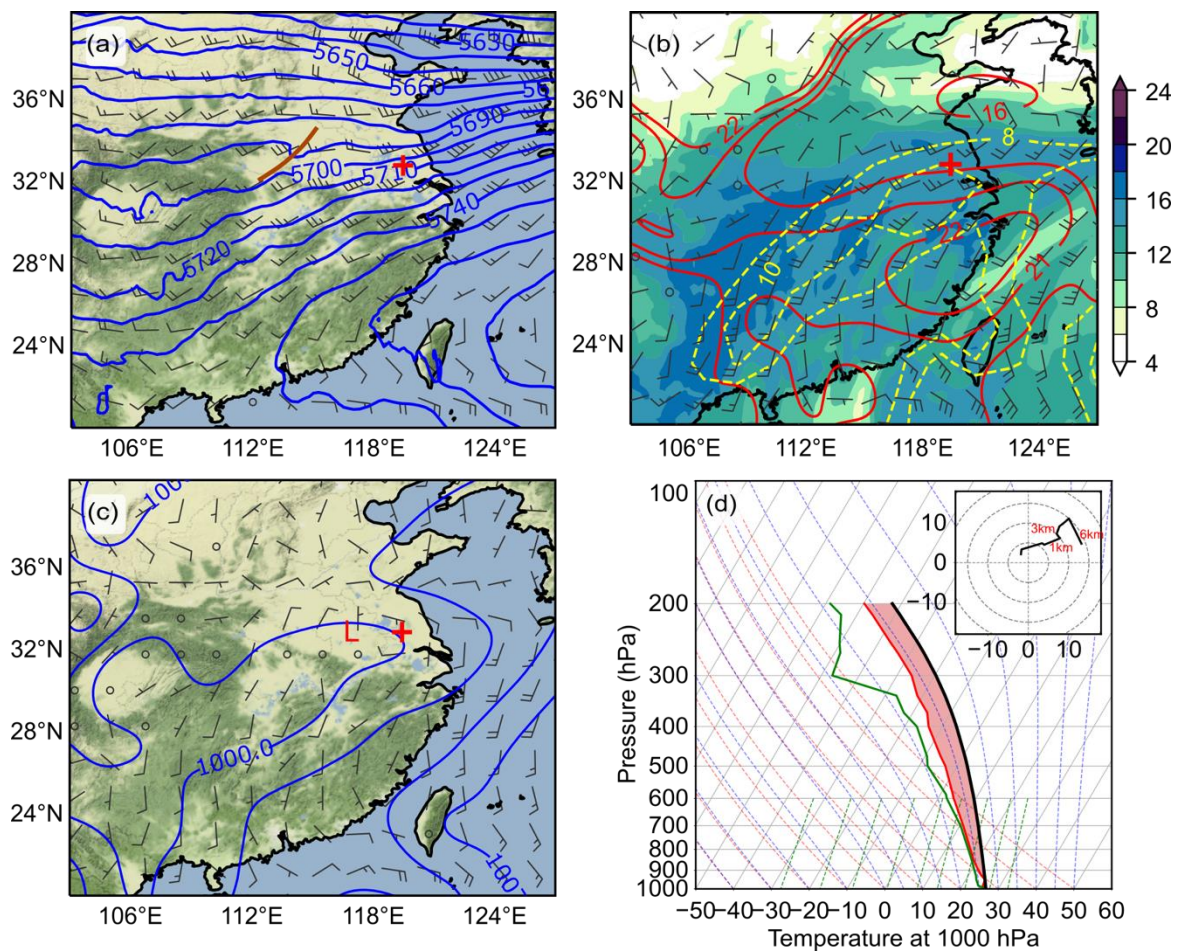


Figure 2. The weather map and the NJ sounding at 0800 LTC on 12 June 2020. (a) Geopotential heights at 500 hPa (the blue contours; gpm), the winds (barbs; m s^{-1}). The brown line shows the weak trough. (b) The winds (barbs; m s^{-1}), temperature (the red contours; $^{\circ}\text{C}$), and the specific humidity (shaded; g kg^{-1}) at 850 hPa. The southwest jets ($>8 \text{ m s}^{-1}$) are marked by yellow contours. (c) Mean sea level pressure (the blue contours; hPa) and the 10 m AGL winds (barbs; m s^{-1}), the “L” marks the location of the low-pressure system. (d) The NJ sounding plotted on a skew T -log P diagram. The temperature T (dewpoint T_d) in $^{\circ}\text{C}$ is shown as the red (green) line. The black line shows the ascending path of a surface-based parcel. The square box in the upper-right corner shows the 0–6 km hodograph with winds in m s^{-1} . Half barbs and full barbs in (a–c) denote 2.5 and 5 m s^{-1} , respectively. The red crosses in (a–c) represent the tornado location.

Table 2. The storm environmental factors based on the NJ sounding, including the convective available potential energy (CAPE), the convective inhibition (CIN), the 0–1 (SRH_{0–1}) and 0–3 (SRH_{0–3}) km storm-relative helicity, and the 0–1 (VWS_{0–1}), 0–3 (VWS_{0–3}), and 0–6 (VWS_{0–6}) km vertical wind shear.

Parameter	Value	Parameter	Value	Parameter	Value
CAPE	1562 J kg ⁻¹	SRH _{0–1}	37 m ² s ⁻²	VWS _{0–1}	7 m s ⁻¹
CIN	−6 J kg ⁻¹	SRH _{0–3}	36 m ² s ⁻²	VWS _{0–3}	7 m s ⁻¹
				VWS _{0–6}	11 m s ⁻¹

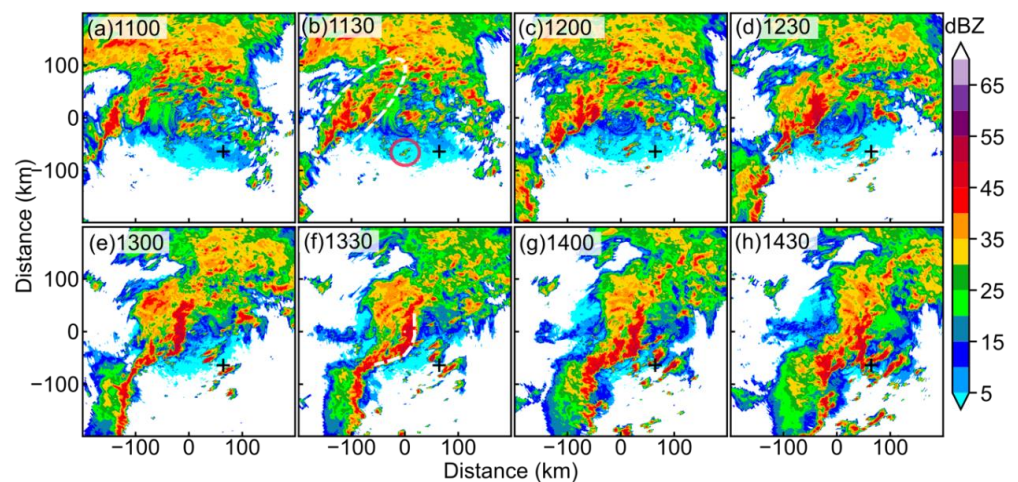


Figure 3. Composite reflectivity fields of the meso- β squall line showing its different stages (a–h) from 1100 to 1430 LTC. The red circle in (b) marks the location of the supercell. The white dashed line in (b) marks the squall line in its early stage. The white dashed line in (f) marks the bow echo of the squall line. The black cross represents the tornado location.

3.2. Evolution of the Squall Line and the Supercell

This tornado was related to two convective systems of different scales, viz. a meso- β squall line and a meso- γ supercell. Figure 3 shows the structure and evolution of the squall line using the composite reflectivity of the HA radar at a 30 min interval. The initial convection of the squall line formed in the northwest of the HA radar before 1100 LTC and slowly evolved into a group of small-scale convective lines (Figure 3b, the white dashed line). The small-scale convective lines later organized into a single convective system by merging convection on the north and south ends (Figure 3c,d). The merged convection continued to intensify and eventually organized into a squall line with a length of about 200 km and a width of about 25 km. At the mature stage of the squall line, a “bow echo” [39] was developed along the outflow boundary in the northern part (Figure 3f, the white dashed line). After 1430 LTC (Figure 3h), the bow echo collapsed, and the squall line entered the dissipation stage. The tornado touchdown around 1355 LTC coincided with the time when the bow echo reached its peak intensity.

Although the meso- β squall line was the predominant feature on the radar echoes, the distance between the squall line and the tornado was greater than 30 km at the closest time (Figure 3g). Therefore, the squall line unlikely contributed to the genesis of this tornado directly. It is noted that an isolated convective cell (the red circle in Figure 3b) with a diameter of about 10 km was initialized about 100 km in front of the developing squall line and was responsible for the formation of this tornado. Figure 4 shows the evolution of radar reflectivity of the supercell from 1300 to 1400 LTC using the HA, NJ, and TZ radars. The reflectivity fields of the three radars were consistent and indicated that the supercell intensified slowly before 1330 LTC. The supercell developed a hook echo (the red dashed circles in Figure 4(d1–d3)) and intensified rapidly after 1330 LTC. The maximum reflectivity

at the tip of the hook echo exceeded 60 dBZ (Figure 4e2). The touchdown location of the tornado corresponds well with the south tip of the supercell (Figure 4f).

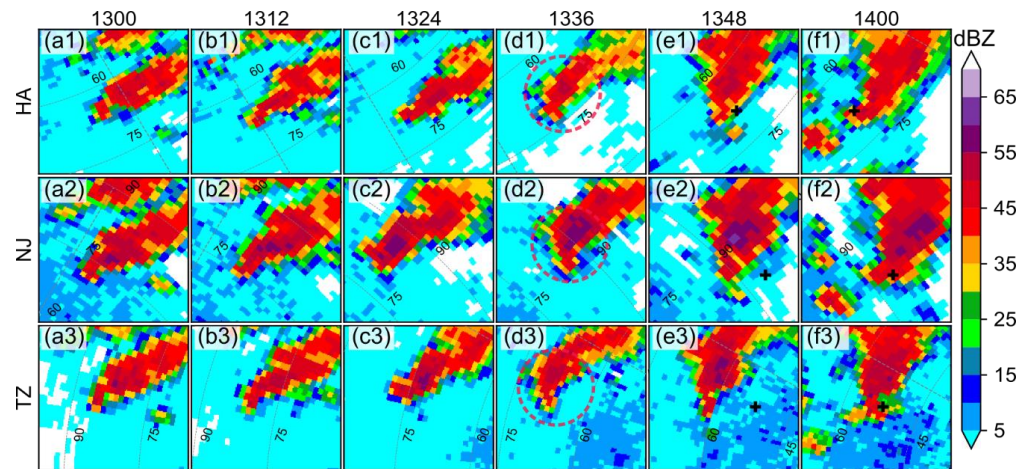


Figure 4. Reflectivity fields of the meso- γ supercell from 1300 to 1400 LTC. Each row (1–3) shows reflectivity fields from one radar at the 0.5° elevation angle, and each column (a–f) shows the supercell at a different time. The red dashed circles in (d) mark the location of the hook echo. The black cross in (e–f) represents the tornado location.

With the evolution of radar reflectivity shown in Figure 4, the supercell developed a cyclonic rotation signature (a dipole in the radial velocity field). As shown in Figure 5, the rotation signature was relatively weak at 1300 LTC with the difference between the maximum outbound and minimum inbound radial velocities about 22 m s^{-1} (Figure 5a). However, the velocity dipole rapidly intensified after 1330 LTC and reached the maximum difference value of 42 m s^{-1} (Figure 5e) at 1348 LTC. After 1400 LTC (not shown), the rotation signature weakened with the dissipation of the supercell. The existence of the hook echo and the rotation signature demonstrated that the meso- γ convective cell was indeed a typical supercell.

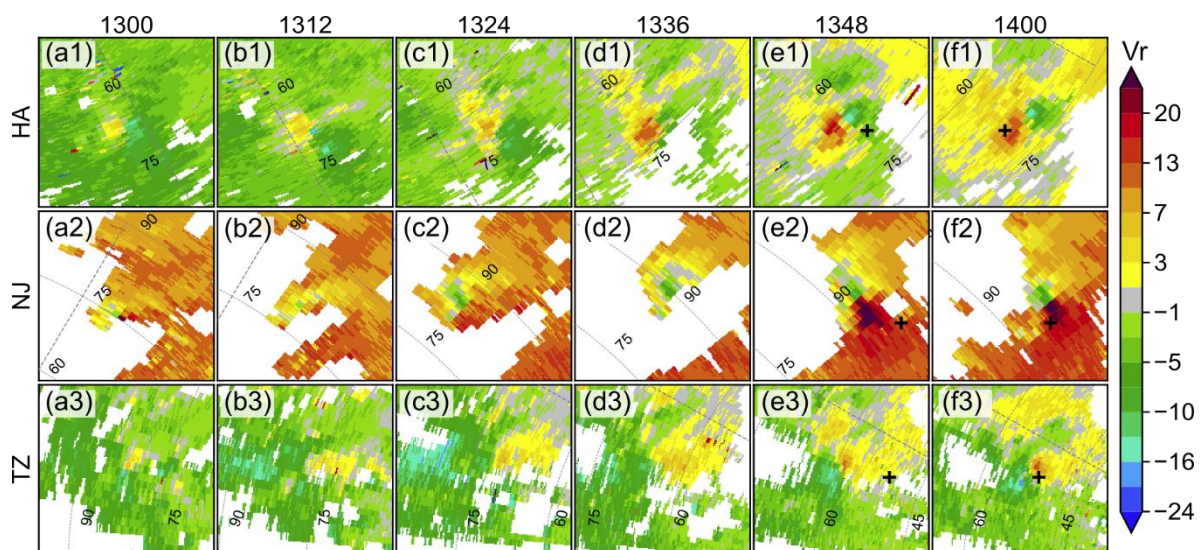


Figure 5. Radial velocity fields of the meso- γ supercell from 1300 to 1400 LTC. Each row (1–3) shows radial velocity fields from one radar at the 0.5° elevation angle, and each column (a–f) shows the supercell at a different time. The black cross in (e–f) represents the tornado location.

3.3. Intensity Evolution of the Supercell

To quantitatively analyze the intensity evolution of the supercell, the azimuthal shear in an area of 40×40 km centered at the radial velocity dipole was estimated at a 6 min interval by the linear least squares derivative method (LLSD) [40]. The evolution of the maximum, mean, and 95% percentile of the azimuthal shear of the radial velocity dipole is shown in Figure 6. Despite some minor differences between the radars, the results show a similar and consistent evolution of azimuthal shear. Before 1330 LTC, the azimuthal shear of the supercell increased slowly with the maximum value below $2.0 \times 10^{-3} \text{ s}^{-1}$ for the HA radar. However, the azimuthal shear increased rapidly after 1330 LTC and reached the maximum values of $3.2 \times 10^{-3} \text{ s}^{-1}$ at 1348 LTC for the HA radar, and $4.0 \times 10^{-3} \text{ s}^{-1}$ at 1400 LTC for the TZ radar. After 1400 LTC, the azimuthal shear weakened rapidly. The quantitative estimation of the azimuthal shear shown in Figure 6 is consistent with the visual inspection of the radial velocities shown in Figure 5. The proximity in time and space between the tornado and the supercell demonstrated that the supercell was the parent storm of this tornado. As the tornado touched down right after the rapid intensification of the supercell, it is interesting to investigate the possible mechanisms for the rapid intensification of the supercell.

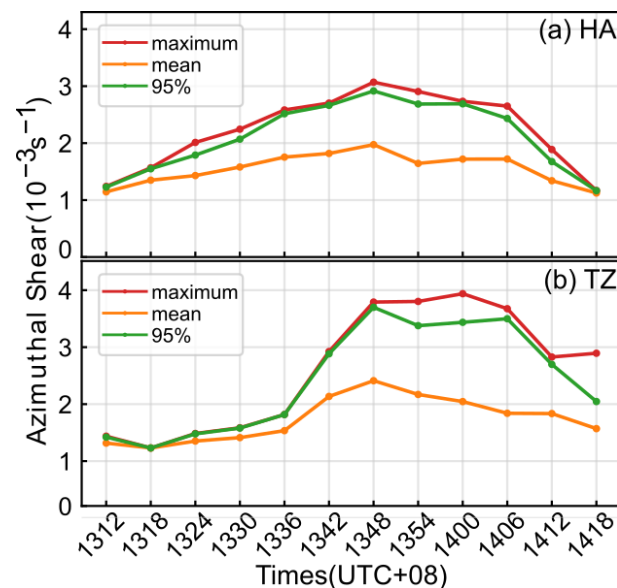


Figure 6. Evolution of the azimuthal shear of the HA (a) and TZ (b) radars at the 0.5° elevation angle from 1312 to 1418 LTC. The red, orange, and green lines are the maximum, mean, and 95% percentile of the azimuthal shear, respectively.

4. Interaction between the Squall Line and the Supercell

It is noted that the parent storm of the tornado, viz. the supercell, was relatively small and weak compared to common tornado-spawn supercells [4,41]. During its first two hours (from 1130 to 1330 LTC) of slow intensification, there was no report of ground damages along its path. The slow intensification of the supercell was consistent with the environment conditions shown in Figure 2. Despite that the values of CAPE and VWS were favorable for the development of convection in general, they were significantly lower than those reported in typical supercell storm environments [21,26,27]. The ERA5 hourly reanalysis showed that the synoptic scale environment was steady (plots not shown), and the sudden intensification of the supercell was not likely attributed to the large-scale environment. As mentioned in the introduction, supercells may intensify through the interaction with other convective systems, which generally enhances the low-level horizontal or vertical vorticity near the supercell [27,28]. To further investigate the possible interaction between the squall line and the supercell, as well as the impact of the interaction on the rapid intensification

of the supercell, the mesoscale and convective-scale wind fields near the supercell were analyzed in more detail.

4.1. The Squall Line

An approaching squall line may modify the local vertical vorticity field due to the wind shear before and after the squall line [23,42]. To further analyze the characteristics of horizontal wind shear associated with the squall line in this case, the vertical wind profiles (VWPs) at the HA, JH, and NJ radars were computed using the DVAD method with an analysis radius of 50 km [43,44]. The analysis radius of 50 km was able to represent the mesoscale mean winds near each radar. The result of the TZ radar was not shown because it was similar to that of the NJ radar. Figure 7 only shows VWPs below 3 km height because the winds above 3 km were consistently westerly. The HA radar (Figure 7a) in the northwest (upstream) of the tornado mainly showed northeasterly and northerly, while the NJ radar (Figure 7c) in the southeast (downstream) of the tornado mainly showed southwesterly and southerly. The VWPs from the HA and NJ radars clearly show that the tornado was spawned in an environment with mesoscale lower-level horizontal wind shear. The JH radar (Figure 7b), which was the closest to the tornado location, showed veering lower-level winds around 1400 LTC. The mean winds at the JH radar were closer to those of the NJ radar before 1400 LTC with a south component, and closer to those of the HA radar afterwards with a north component. The veering lower-level winds indicate that the mesoscale horizontal shear associated with the squall line was approaching the tornado location when the tornado made touchdown. The approaching mesoscale horizontal shear may enhance the background vertical vorticity near the supercell and contribute to the intensification of the supercell [45].

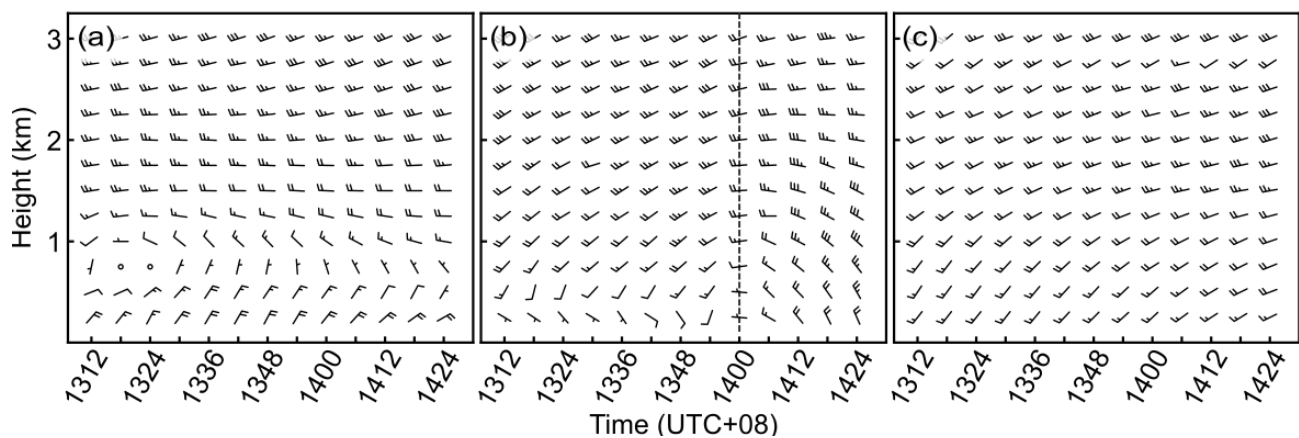


Figure 7. Time series of VWPs computed from the HA (a), JH (b), and NJ (c) radars from 1312 to 1424 LTC. The half and full wind barbs represent 2.5 m s^{-1} and 5 m s^{-1} , respectively. The dashed line in (b) marks the time of the veering lower-level winds.

4.2. The Bow Echo

As shown in Figure 3g, the tornado was spawned when the bow echo of the approaching squall line reached its mature stage. The development of bow echoes often generates storm-scale meso-vortices along the cold outflow boundaries [46]. Previous studies [23,24,27] have shown that these meso-vortices may play an important role in the genesis of tornadoes. As the bow echo remained more than 30 km away from the tornado, it is not likely attributed to the genesis of this tornado directly. However, the approaching bow echo may have indirectly contributed to the tornadogenesis by modifying the local environment of the supercell. In order to understand the possible impact of the bow echo, the retrieved three-dimensional winds at 1 km height from 1318 to 1354 LTC are shown in Figure 8. The wind fields at these three times were similar, with southwesterly and westerly on the southeast and northwest side of the squall line, respectively. The northeast end of the

bow echo developed a cyclonic vortex (bookend vortex) [47]. There was a strong northwest rear inflow jet (RIJ) perpendicular to the orientation of the bow echo on the southwest side of the cyclonic vortex. The increased momentum due to the RIJ may modify the wind fields in front of the bow echo and impact the evolution of the supercell.

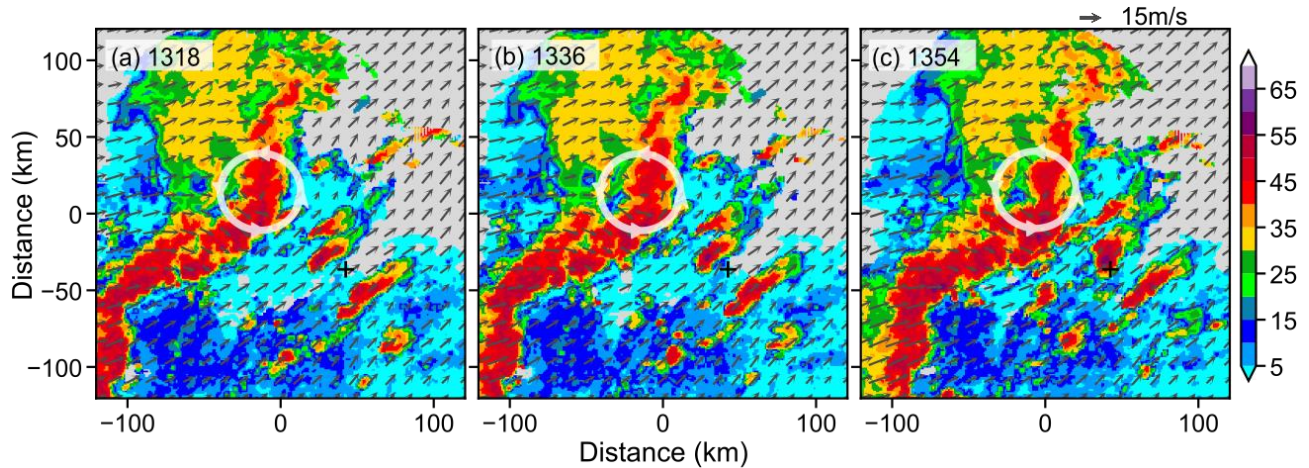


Figure 8. Retrieved horizontal winds (vector) and reflectivity (shaded) near the tornado location on 1 km height at 1318 (a), 1336 (b) and 1354 (c) LTC. The white circle represents the bookend vortex. The black cross represents the tornado location.

Figure 9 shows the wind fields and vertical vorticity at 3 km height at the same time as Figure 8. There was a couplet of vertical vorticity at the south tip of the supercell. Given a northeast environmental VWS shown in Figure 2d, the vertical vorticity couplet is oriented perpendicular to the environmental VWS and is consistent with the process of vertical vorticity generation by tilting of the horizontal vorticity [48–50]. The strength of the positive vertical vorticity appeared to be intensifying as the bow echo moved closer, which is consistent with the increase of azimuth shear shown in Figure 6.

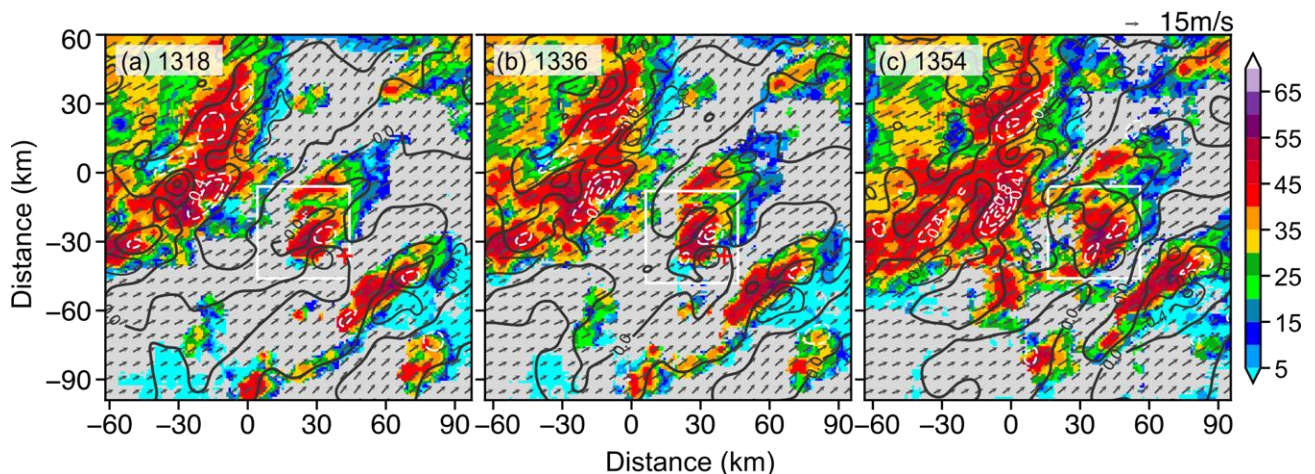


Figure 9. Evolution of the vertical vorticity (contours), horizontal winds (vector), and reflectivity (shaded) on 3 km height at 1318 (a), 1336 (b) and 1354 (c) LTC. The white (black) contours are negative (positive) vorticity, and the bold black contours indicate the value of 0. The red cross represents the tornado location. The white box is the VWP analysis area.

To quantify the modification to the local wind fields of the supercell by the approaching bow echo, the VWPs averaged over a region of 40×40 km centered at the supercell (the white box in Figure 9) are shown in Figure 10. The VWPs at different times show intensifying lower-level winds, especially below 6 km height. The u and v winds increased

by 1 m s^{-1} and 2 m s^{-1} at 1 km height, respectively. As the evolution of supercell is closely related to the VWP of the local environment [51,52], the enhancement of local winds may promote the intensification of the supercell.

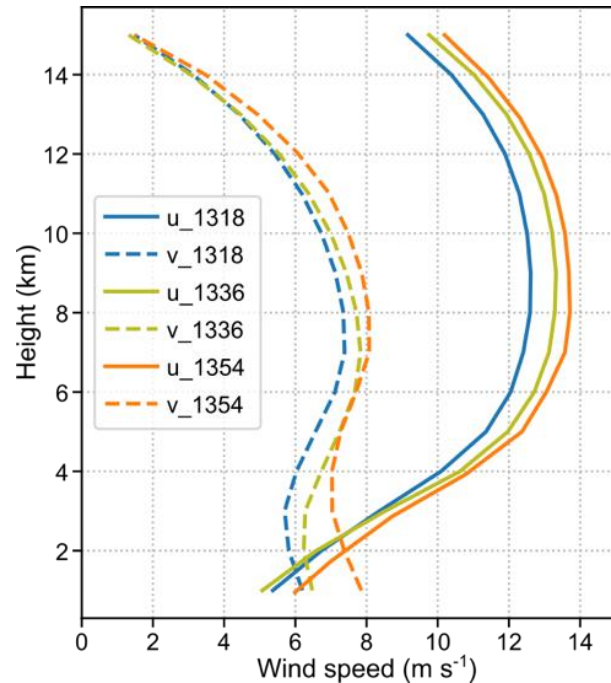


Figure 10. The VWPs of the retrieved three-dimensional winds averaged over a region of $40 \times 40 \text{ km}$ centered at the supercell at 1318 LTC (blue), 1336 LTC (green), and 1354 (orange) LTC.

The evolution of midlevel rotation in supercells is relatively well understood, which can be explained by the following linear theory of midlevel mesocyclogenesis [15]:

$$\left(\frac{\partial \zeta'}{\partial t}\right)_{sr} = -(\bar{V} - C) \cdot \nabla_h \zeta' + S \times \nabla w' \cdot k \tag{9}$$

where S is the 0–3 km mean VWS, \bar{V} is the 0–6 km mean horizontal wind, C is the mean translation vector of the supercell updraft, k is the unit vector in the vertical, and ζ' and w' are the perturbation of vertical vorticity and vertical velocity, respectively. Equation (9) is essentially the linearized version of the vertical vorticity equation written in the moving frame of a supercell. As the terms on the RHS of Equation (9) can be estimated given a VWP near the storm, this equation has been widely used in the diagnosis and forecasting of the evolution of supercell storms [53,54].

The radar reflectivity fields and the VWPs shown in Figures 8 and 10 were used to estimate the terms on the RHS of Equation (9), and further evaluate the impact of the enhanced lower-level winds on the intensification of the supercell in this case. The estimated S , \bar{V} , and C at 1318 and 1354 LTC were shown in Figure 11. Note that the multi-radar wind retrieval was not able to recover the winds below 1 km height, which were estimated by the ERA5 hourly reanalysis. As illustrated in Figure 11, both S and \bar{V} vectors are directed towards the northeast, with S to the right of the \bar{V} . The C further veered towards the east. The enhanced lower-level winds at 1354 LTC increased the magnitudes of both the S and \bar{V} . According to Equation (9), the increase of S is able to increase the local vorticity by the tilting process [15]. The translation speed (C) also increased substantially with the increase of lower-level winds. The change of \bar{V} and C resulted in a greater component of the storm-relative wind ($\bar{V} - C$) perpendicular to the S . The increased streamwise vorticity could further help to align the positive vertical vorticity center generated by the tilting process with the updraft core and promote the intensification of the supercell [48,49]. The

effect of the enhanced lower-level winds on the supercell can be also accessed by the dynamic parameters shown in Table 3. The VWSs and SRHs were increasing with time and were generally stronger than those derived from the sounding (Table 2). In summary, the enhanced lower-level winds associated with the approaching bow echo increased the crosswise and streamwise vorticity components of the storm-relative velocity vector near the supercell, which is favorable for the rapid intensification of the supercell. The rapidly intensified supercell then led to the subsequent tornadogenesis.

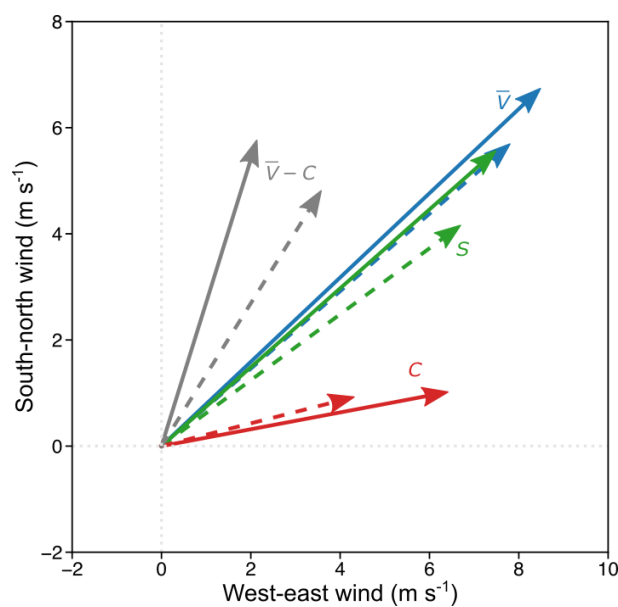


Figure 11. Wind vectors related to the intensification of the supercell at 1318 (dashed lines) and 1354 (solid lines) LTC, respectively. The grey ones represent the storm-relative winds ($\bar{V} - C$), the blue ones represent the 0–6 km mean horizontal winds (\bar{V}), the green ones represent the 0–3 km mean VWSs (S), and the red ones represent the mean translation vectors of the supercell updraft (C).

Table 3. The local environmental factors based on the VVPs in Figure 11, including the 0–1 (VWS₀₋₁), 0–3 (VWS₀₋₃), and the 0–6 (VWS₀₋₆) km vertical wind shear, and the 0–1 (SRH₀₋₁) and 0–3 (SRH₀₋₃) km storm-relative helicity.

Time	VWS ₀₋₁	VWS ₀₋₃	VWS ₀₋₆	SRH ₀₋₁	SRH ₀₋₃
1318	6 m s ⁻¹	8 m s ⁻¹	12 m s ⁻¹	33 m ² s ⁻²	46 m ² s ⁻²
1336	6 m s ⁻¹	9 m s ⁻¹	13 m s ⁻¹	36 m ² s ⁻²	52 m ² s ⁻²
1354	8 m s ⁻¹	10 m s ⁻¹	13 m s ⁻¹	48 m ² s ⁻²	67 m ² s ⁻²

5. Discussion and Summary

The “0612” Gaoyou tornado was spawned in a favorable synoptic environment with moderate unstable energy and veering VWS. A noteworthy aspect of this tornado is that its formation was associated with two convective systems of different scales. The larger system, viz. the meso-β squall line, formed about three hours prior to the tornado touchdown and developed a predominant bow echo at its mature stage. Due to the large distance between the squall line and the tornado, the squall line was believed to be not directly related to the formation of the tornado. A smaller meso-γ supercell initialized in the front of the squall line two and half hours before the tornado touchdown was the parent storm of this tornado. The supercell underwent slow intensification in the first two hours without causing any damage near its path. However, the supercell intensified rapidly in the last half an hour and finally led to the tornado documented in this paper.

The rapid intensification of the parent supercell and the subsequent tornadogenesis was attributed to the interaction of the squall line and the supercell. The VVPs retrieved by the

single doppler radars showed a lower-level mesoscale horizontal shear zone associated with the squall line, which helped to increase the environment vertical vorticity near the supercell. The formation of the bow echo and its catching-up with the supercell modified the kinematic fields near the supercell. The accelerated lower-level winds enhanced the tilting and stretching processes by increasing the crosswise and streamwise vorticity components. In summary, the interactions between the squall line and the supercell contributed to the rapid intensification of the supercell and may have played a role in the subsequent tornadogenesis.

This study showed the complex interactions on the parent storm of tornadoes and their possible impact on tornadogenesis. However, limited by the available observations, the hypothesis proposed in this study is subjected to uncertainty and needs to be further verified by more observational and numerical studies. It is worth noting that other mechanisms, including the self-organization of supercells and thermodynamic processes, could also have played a role in the intensification of the supercell documented in this study. As the investigation of other mechanisms is not supported by the current dataset, this study has no intention to downplay or disprove the importance of other possible processes. Despite these limitations, this study demonstrated the value of better understanding the interaction between larger storms associated with tornadoes in order to accurately monitor and predict the occurrence of tornadoes.

Author Contributions: Conceptualization, X.T.; data curation, F.X.; funding acquisition, F.Z.; project administration, F.Z.; writing—original draft, J.T.; writing—review and editing, J.T. and X.T. All authors have read and agreed to the published version of the manuscript.

Funding: This work was funded by the National Key Research and Development Project of China (2018YFC1506103) and the National Natural Science Foundation of China (Grant 41505045).

Data Availability Statement: Due to confidentiality agreements, supporting data can only be made available to bona fide researchers subject to a non-disclosure agreement. Details of the data and how to request access are available from <https://tornado.cuit.edu.cn/data> (accessed on 1 December 2021).

Acknowledgments: Thanks to Jiangsu Meteorological Bureau for providing disaster survey information.

Conflicts of Interest: The authors declare no conflict of interest.

References

1. Brooks, H.E.; James, W.L.; Jeffrey, P.C. The Spatial Distribution of Severe Thunderstorm and Tornado Environments from Global Reanalysis Data. *Atmos. Res.* **2003**, *67*, 73–94. [[CrossRef](#)]
2. Fan, W.J.; Yu, X.D. Characteristics of Spatial-Temporal Distribution of Tornadoes in China. *Meteorol. Mon.* **2015**, *41*, 793–805.
3. Bai, L.Q.; Meng, Z.Y.; Huang, L.; Yan, L.J.; Li, Z.H.; Mai, X.H.; Huang, Y.P.; Yao, D.; Wang, X. An Integrated Damage, Visual, and Radar Analysis of the 2015 Foshan, Guangdong, EF3 Tornado in China Produced by the Landfalling Typhoon Mujigae (2015). *Bull. Am. Meteorol. Soc.* **2017**, *98*, 2619–2640. [[CrossRef](#)]
4. Meng, Z.Y.; Bai, L.Q.; Zhang, M.R.; Wu, Z.F.; Li, Z.H.; Pu, M.J.; Zheng, Y.G.; Wang, X.H.; Yao, D.; Xue, M.; et al. The Deadliest Tornado (EF4) in the Past 40 Years in China. *Weather Forecast.* **2018**, *33*, 693–713. [[CrossRef](#)]
5. Hirth, B.D.; Schroeder, J.L.; Weiss, C.C. Surface Analysis of the Rear-Flank Downdraft Outflow in Two Tornadic Supercells. *Mon. Weather Rev.* **2008**, *136*, 2344–2363. [[CrossRef](#)]
6. Karstens, C.D.; Samaras, T.M.; Lee, B.D.; Gallus, W.A.; Finley, C.A. Near-Ground Pressure and Wind Measurements in Tornadoes*. *Mon. Weather Rev.* **2010**, *138*, 2570–2588. [[CrossRef](#)]
7. Edwards, R.; LaDue, J.G.; Ferree, J.T.; Scharfenberg, K.; Maier, C.; Coulbourne, W.L. Tornado Intensity Estimation: Past, Present, and Future. *Bull. Am. Meteorol. Soc.* **2013**, *94*, 641–653. [[CrossRef](#)]
8. Stout, G.E.; Huff, F.A. Radar Records Illinois Tornadogenesis. *Bull. Am. Meteorol. Soc.* **1953**, *34*, 281–284.
9. Garrett, R.A.; Rockney, V.D. Mornadoes in northeastern Kansas, May 19, 1960. *Mon. Weather Rev.* **1962**, *90*, 231–240. [[CrossRef](#)]
10. Donaldson, R.J. Vortex Signature Recognition by a Doppler Radar. *J. Appl. Meteorol.* **1970**, *9*, 661–670. [[CrossRef](#)]
11. Brown, R.A.; Lemon, L.R.; Burgess, D.W. Tornado Detection by Pulsed Doppler Radar. *Mon. Weather Rev.* **1978**, *106*, 29–38. [[CrossRef](#)]
12. Stumpf, G.J.; Witt, A.; Mitchell, E.D.; Spencer, P.L.; Johnson, J.T.; Eilts, M.D.; Thomas, K.W.; Burgess, D.W. The National Severe Storms Laboratory Mesocyclone Detection Algorithm for the WSR-88D*. *Weather Forecast.* **1998**, *13*, 304–326. [[CrossRef](#)]
13. Mitchell, E.; Vasiloff, S. The national severe storms laboratory tornado detection algorithm. *Weather Forecast.* **1998**, *13*, 352–366. [[CrossRef](#)]

14. Trapp, R.J.; Tessendorf, S.A.; Godfrey, E.S.; Brooks, H.E. Tornadoes from Squall Lines and Bow Echoes. Part I: Climatological Distribution. *Weather Forecast.* **2005**, *20*, 23–34. [[CrossRef](#)]
15. Markowski, P.; Richardson, Y. *Mesoscale Meteorology in Midlatitudes*; John Wiley & Sons, Ltd.: Hoboken, NJ, USA, 2010; pp. 32–33. ISBN 978-047-074-213-6.
16. Forbes, G.S. On the Reliability of Hook Echoes as Tornado Indicators. *Mon. Weather Rev.* **1981**, *109*, 1457–1466. [[CrossRef](#)]
17. Trapp, R.J.; Stumpf, G.J.; Manross, K.L. A Reassessment of the Percentage of Tornadic Mesocyclones. *Weather Forecast.* **2005**, *20*, 680–687. [[CrossRef](#)]
18. Burgess, D.W.B.; Donaldson, R.J.; Desrochers, P.R. Tornado detection and warning by radar. In *Geophysical Monograph Series*; Church, C., Burgess, D., Doswell, C., Davies-Jone, R., Eds.; American Geophysical Union: Washington, DC, USA, 1993; Volume 79, pp. 203–221.
19. Wakimoto, R.M.; Wilson, J.W. Non-supercell Tornadoes. *Mon. Weather Rev.* **1989**, *117*, 1113–1140. [[CrossRef](#)]
20. Brady, R.H.; Szoke, E.J. A Case Study of Nonmesocyclone Tornado Development in Northeast Colorado: Similarities to Waterspout Formation. *Mon. Weather Rev.* **1989**, *117*, 843–856. [[CrossRef](#)]
21. Funk, T.W.; Darmofal, K.E.; Kirkpatrick, J.D.; DeWald, V.L.; Przybylinski, R.W.; Schmocker, G.K.; Lin, Y.-J. Storm Reflectivity and Mesocyclone Evolution Associated with the 15 April 1994 Squall Line over Kentucky and Southern Indiana. *Weather Forecast.* **1999**, *14*, 976–993. [[CrossRef](#)]
22. DeWald, V.L.; Funk, T.W. WSR-88D reflectivity and velocity trends of a damaging squall line event on 20 April 1996 over south-central Indiana and central Kentucky. In Proceedings of the 20th Conference on Severe Local Storms, Orlando, FL, USA, 11–15 September 2000.
23. Trapp, R.J.; Weisman, M.L. Low-Level Mesovortices within Squall Lines and Bow Echoes. Part II: Their Genesis and Implications. *Mon. Weather Rev.* **2003**, *131*, 2804–2823. [[CrossRef](#)]
24. Atkins, N.T.; Laurent, M.S. Bow Echo Mesovortices. Part I: Processes That Influence Their Damaging Potential. *Mon. Weather Rev.* **2009**, *137*, 1497–1513. [[CrossRef](#)]
25. Penn, S.; Pierce, C.; McGuire, J.K. The Squall Line and Massachusetts Tornadoes of June 9, 1953. *Bull. Am. Meteorol. Soc.* **1955**, *36*, 109–122. [[CrossRef](#)]
26. Goodman, S.J.; Knupp, K.R. *Tornadogenesis via Squall Line and Supercell Interaction: The November 15, 1989, Huntsville, Alabama, Tornado, in the Tornado: Its Structure, Dynamics, Prediction, and Hazards*; Church, C., Burgess, D., Dosewell, C., Davies-Jone, R., Eds.; American Geophysical Union: Washington, DC, USA, 1993; Volume 79, pp. 183–199. ISBN 978-087-590-038-4.
27. Wolf, P.L. WSR-88D Radar Depiction of Supercell–Bow Echo Interaction: Unexpected Evolution of a Large, Tornadic, “Comma-Shaped” Supercell over Eastern Oklahoma. *Weather Forecast.* **1998**, *13*, 492–504. [[CrossRef](#)]
28. French, A.J.; Parker, M.D. Observations of Mergers between Squall Lines and Isolated Supercell Thunderstorms. *Weather Forecast.* **2012**, *27*, 255–278. [[CrossRef](#)]
29. Yao, Y.; Yu, X.; Zhang, Y.; Zhou, Z.; Xie, W.; Lu, Y.; Yu, J.; Wei, L. Climate analysis of tornadoes in China. *J. Meteorol. Res.* **2015**, *29*, 359–369. [[CrossRef](#)]
30. Barga, D.W.; Brown, R.C. Interactive Radar Velocity Unfolding. In Proceedings of the 19th Conference on Radar Meteorology, Miami Beach, FL, USA, 15–18 April 1980; Volume 60, pp. 1485–1519.
31. Steiner, M.; Smith, J.A. Use of Three-Dimensional Reflectivity Structure for Automated Detection and Removal of Nonprecipitating Echoes in Radar Data. *J. Atmos. Ocean. Technol.* **2002**, *19*, 673–686. [[CrossRef](#)]
32. Bell, M.M.; Lee, W.-C.; Wolff, C.A.; Cai, H. A Solo-Based Automated Quality Control Algorithm for Airborne Tail Doppler Radar Data. *J. Appl. Meteorol. Climatol.* **2013**, *52*, 2509–2528. [[CrossRef](#)]
33. Lee, W.-C.; Tang, X.; Jou, B.J.-D. Distance Velocity–Azimuth Display (DVAD)—New Interpretation and Analysis of Doppler Velocity. *Mon. Weather Rev.* **2014**, *142*, 573–589. [[CrossRef](#)]
34. Tang, X.; Lee, W.-C.; Wang, Y. Nonlinear Wind Analysis of Single-Doppler Radar Observations within a DVAD Framework. *J. Appl. Meteorol. Climatol.* **2015**, *54*, 1538–1555. [[CrossRef](#)]
35. Gamache, J.F. Evaluation of a fully-three dimensional variational Doppler analysis technique. In Proceedings of the 28th Conference on Radar Meteorology, Austin, TX, USA, 7–12 September 1997; pp. 422–423.
36. Edwards, R.; Thompson, R.L. RUC-2 supercell proximity soundings, Part II: An independent assessment of supercell forecast parameters. In Proceedings of the 20th Conference on Severe Local Storms, Orlando, FL, USA, 11–15 September 2000.
37. Thompson, R.L.; Edwards, R.; Hart, J.A.; Elmore, K.L.; Markowski, P. Close Proximity Soundings within Supercell Environments Obtained from the Rapid Update Cycle. *Weather Forecast.* **2003**, *18*, 1243–1261. [[CrossRef](#)]
38. Resmussen, E.N. Refined supercell and tornado forecast parameters. *Weather Forecast.* **2003**, *18*, 530–535. [[CrossRef](#)]
39. Weisman, M.L. Bow Echoes: A Tribute to T. T. Fujita. *Bull. Am. Meteorol. Soc.* **2001**, *82*, 97–116. [[CrossRef](#)]
40. Smith, T.M.; Elmore, K. The use of radial velocity derivative to diagnose rotation and divergence. In Proceedings of the 11th Conference on Aviation, Range and Aerospace, Hyannis, MA, USA, 3–8 October 2004.
41. Palmer, R.D.; Bodine, D.; Kumjian, M.; Cheong, B.; Zhang, G.; Cao, Q.; Bluestein, H.B.; Ryzhkov, A.; Yu, T.-Y.; Wang, Y. Observations of the 10 May 2010 Tornado Outbreak Using OU-PRIME: Potential for New Science with High-Resolution Polarimetric Radar. *Bull. Am. Meteorol. Soc.* **2011**, *92*, 871–891. [[CrossRef](#)]
42. Noda, A.T.; Niino, H. Genesis and Structure of a Major Tornado in a Numerically-Simulated Supercell Storm: Importance of Vertical Vorticity in a Gust Front. *SOLA* **2005**, *1*, 5–8. [[CrossRef](#)]

43. Li, N.; Wei, M.; Tang, X.; Pan, Y. An improved velocity volume processing method. *Adv. Atmos. Sci.* **2007**, *24*, 893–906. [[CrossRef](#)]
44. Chrisman, J.; Smith, S. Enhanced Velocity Azimuth Display Wind Profile (EVWP) Function for the WSR-88D. In Proceedings of the 34th Conference on Radar Meteorology, Williamsburg, VA, USA, 5–9 October 2009.
45. Lee, B.D.; Wilhelmson, R.B. The Numerical Simulation of Non-Supercell Tornadogenesis. Part I: Initiation and Evolution of Pretornadic Misocyclone Circulations along a Dry Outflow Boundary. *J. Atmos. Sci.* **1997**, *54*, 32–60. [[CrossRef](#)]
46. Schenkman, A.D.; Xue, M. Bow-echo mesovortices: A review. *Atmos. Res.* **2016**, *170*, 1–13. [[CrossRef](#)]
47. Weisman, M.L. The Genesis of Severe, Long-Lived Bow Echoes. *J. Atmos. Sci.* **1993**, *50*, 645–670. [[CrossRef](#)]
48. Davies-Jones, R. Streamwise Vorticity: The Origin of Updraft Rotation in Supercell Storms. *J. Atmos. Sci.* **1984**, *41*, 2991–3006. [[CrossRef](#)]
49. Davies-Jones, R.; Trapp, R.J.; Bluestein, H.B. Tornadoes and Tornadic Storms. In *Severe Convective Storms, Boston*; Meteorological Society: Boston, MA, USA, 2001; pp. 167–221.
50. Dahl, J.M.L. Tilting of Horizontal Shear Vorticity and the Development of Updraft Rotation in Supercell Thunderstorms. *J. Atmos. Sci.* **2017**, *74*, 2997–3020. [[CrossRef](#)]
51. Rotunno, R.; Klemp, J.B. The Influence of the Shear-Induced Pressure Gradient on Thunderstorm Motion. *Mon. Weather Rev.* **1982**, *110*, 136–151. [[CrossRef](#)]
52. Rotunno, R.; Klemp, J.B. On the Rotation and Propagation of Simulated Supercell Thunderstorms. *J. Atmos. Sci.* **1985**, *42*, 271–292. [[CrossRef](#)]
53. Thompson, R.L.; Mead, C.M.; Edwards, R. Effective Storm-Relative Helicity and Bulk Shear in Supercell Thunderstorm Environments. *Weather Forecast.* **2007**, *22*, 102–115. [[CrossRef](#)]
54. Davenport, C.E. Environmental Evolution of Long-Lived Supercell Thunderstorms in the Great Plains. *Weather Forecast.* **2021**, *36*, 2187–2209. [[CrossRef](#)]